Discharge rate characterization for submerged grains flowing through a hopper using DEM-LBM simulations

Jianhua Fan, Li-Hua Luu, Pierre Philippe, Gildas Noury

A dimensional analysis for submerged granular discharge from hoppers using DEM-LBM simulations

Jianhua Fan[a,*], Li-Hua Luu[b], Pierre Philippe[b], Gildas Noury[c]

[a] *School of Mechanical and Aerospace Engineering, Jilin University, 130025 Changchun, China*
[b] *RECOVER, INRAE Aix-Marseille University, 3275 route de Cézanne, 13182 Aix-en-Provence, France*
[c] *BRGM, DRP, 3 avenue Claude Guillemin, 45060 Orléans, France*

Abstract

In the context of sinkhole occurrences during a flood due to the presence of underground conduits, submerged granular flows through an orifice have been numerically investigated. To account for the fluid-solid interaction at the pore-scale, we use a numerical modelling that combines the Discrete Element Method (DEM) for the solid particles with the Lattice Boltzmann Method (LBM) for the fluid dynamics. We performed a parametric study by varying particles diameter, fluid viscosity and hopper orifice size, enabling the exploration of the Archimedes number over five orders of magnitude. Solid discharge rates, that are shown to depend on the hydraulic boundary conditions, are nevertheless predictable by an extension of the classical Beverloo law. Finally, we present a primary study of the submerged grains velocity profiles at the orifice that includes a comparison with recent experimental results (Koivisto & Durian, 2017) and a discussion on fluid entrainment by the downward granular flow.

Keywords: Granular flow, Hopper, Sinkhole, LBM-DEM

1. Introduction

A prominent problem in granular matter is that of hopper and silo discharge in which grains typically flow at a constant rate. Numerous researches have been made in the past that investigated different types of granular flows through a bottom outlet, with important applications in several industries such as mining, agriculture, food, or pharmaceutical [1, 2, 3, 4, 5, 6]. Though dry grains discharge is rather well predicted, the potential behavior change when adding interstitial liquid, from partially to fully saturated situation, was much less studied. Nevertheless, the submerged granular flows are significantly encountered in geophysical processes such as soil subsidence after floods, which may occurs with increasing frequency due to climate changes [7, 8, 9]. In the case of intense rainfall, karst cover soils turn out to be one of the most critical environments for sinkhole occurrence [10, 11]. The presence of flooded underground conduits actually induces a downward washing of the ground soil into the network of limestone cavities *via* water circulation [12].

In this paper, we propose to focus on submerged granular flows through an orifice with the aim of improving our knowledge of hydro-mechanical instabilities responsible for sinkhole hazards but also, more broadly, to investigate how far the presence of an interstitial liquid can affect the classical dry granular discharge. Concerning the latter and more common situation, pioneering works have established an empirical relationship based on the picture of transient arches that form and break over the hole, leaving the grains (of diameter d) to fall freely from a distance proportional to the orifice size. Consequently, the discharge simply scales as the product of the free fall velocity $(gD)^{1/2}$ and the outlet area. Thus, the mass flow rates from bottom exits in cylindrical hoppers follow the so-called Beverloo law, which reads:

$$Q = C\rho g^{1/2}(D - kd)^{5/2}, \tag{1}$$

where D is the orifice size, d is the mean diameter of the grains, $g = 9.81\ m.s^{-2}$ is gravity, k is a dimensionless constant with typical values $k \approx 1 - 2$, and C is a dimensionless flowability coefficient which usually has a value close to 1 [1, 13]. The cut-off parameter k determines an apparent orifice $D - kd$ that includes an empty surrounding annulus assumed to be unreachable by the grains.

A striking (and of practical interest for the ancient hourglass) feature of the classical dry hopper discharge, is certainly the achievement of a constant flow rate regardless of the overlying height of grains. For this reason, many studies have investigated the transmission of forces through the dynamic granular contact network [14]. Tang & Behringer [15] first used a 2D-hopper filled with photoelastic particles to enable direct visualization of the force chains creating arches perpendicularly to the flow streamlines. For a 3D-hopper, stress measurements can be acquired by means of pressure sensors, but remain limited to wall normal stress data [16]. In a complementary approach, numerical simulations by the discrete element method (DEM) have been extensively used to study dry granular flows from silos in the last decade and have provided a much more detailed description of flow quantities which are difficult, or either im-

*corresponding author
Email address: jianhua_*fan*@jlu.edu.cn (Jianhua Fan)

possible, to evaluate experimentally. For instance, Langston *et al*. [17] investigated the stress field in funnel hopper flows, while Masson & Martinez [18] also employed DEM simulations to demonstrate the influence of friction and stiffness at contacts in silo flows. Ketterhagen *et al*. [19] also succeeded in assessing hoppers performance thanks to the numerical measurement of some internal parameters, such as the particle residence times and the particle velocities, during discharge. A recent progress is the evidence of self-similar velocity profiles at the outlet [5, 20]. However, to our knowledge, this finding has not been reported under submerged conditions. More generally, only limited studies have examined the influence of the interstitial fluid on granular dynamics. This research mainly concerns gas-assisted discharge through an orifice [2, 3, 21, 22]. In particular, rather few experimental works specifically concern hopper flow of water submerged systems [23, 24, 26, 27, 28].

For submerged granular hoppers, Wilson *et al.* [24] experimentally validated a very similar approach where the previous Beverloo law is straightforwardly generalized by using now the terminal falling velocity of the grains and thus accounting for fluid drag. In a previous work, the present authors numerically investigated granular discharge through an aperture, in 2D geometry and totally saturated condition, using LBM-DEM approach, that combines the lattice Boltzmann method for describing the fluid phase and the discrete element method for the solid phase [25]. A similar Beverloo-like prediction for the solid flow rate was found, where the interstitial fluid contribution is given by a higher orifice cut-off k than for the dry case. In this paper, we now intend to examine the influence of the fluid properties (primarily its viscosity) on the discharge rate and its crucial coupling with the particles. Note that from this perspective, Koivisto & Durian [26] notably highlighted in their experiments a final surge caused by a self-induced pumping of fluid through the granular medium. Moreover, the surrounding liquid is found to reduce friction between the grains and thus promote jamming at the outlet [27, 28]. These recent results emphasizing the poro-mechanical coupling are reminiscent of the phenomenology of granular column in fluid, whose dynamics is strongly controlled by the initial packing fraction through dilatancy or contractancy [29, 30].

The main goal of this paper is to numerically study the impact of the addition of a liquid during a process of grains discharge through an orifice using DEM-LBM simulations. This coupling approach provides a micro-mechanical insight by giving access not only to both solid particles and liquid flows, but also to the internal stress field. The paper is organized as follows. The coupled fluid-solid numerical scheme implemented in the framework of the coupled lattice Boltzmann and discrete element methods is first introduced in Section 3. The simulations of submerged granular flows following a dimensionless parametric study of the solid discharge rates are presented in Section 4. Then, we propose an analysis of the results with a specific scope on fluid-grains coupling in Section 5. Finally, Section 6 gives the conclusion and some outlooks for future investigations.

2. Numerical methods

3. Numerical methods

Over the last ten years, a growing number of numerical studies have relied on schemes that couple Discrete Element Method (DEM) with Lattice Boltzmann method (LBM) to tackle many different multi-scale geomechanical issues [12, 31, 32, 42, 43]. This section dedicated to a brief description of the version of this coupling method used here (more details are presented in [43])

3.1. Fluid phase modeling: Lattice Boltzmann Method (LBM)

As one of the computational fluid dynamic approach that can retrieve the Navier-Stokes equations with a Chapman-Enskog expansion, LBM derives from lattice gas cellular automata model. Its computational domain is discretized on a regular lattice grid with a given spatial interval. The fluid flow is simulated based on the resolution of a discretized form of the Boltzmann equation (see Eq 3) which rules the time evolution for the probability function $f_i(\vec{x}, t)$ to find a virtual fluid particle moving with velocity $\vec{e}_i$ located at the position $\vec{x}$ and at the given time t. Here we employ a two-dimensional space with nine velocities at each grid called D2Q9 model [33] and whose the discrete velocities $\vec{e}_i$ are defined by:

$$\vec{e}_i = \begin{cases} (0,0) & (i=0) \\ c(\cos\dfrac{\pi(i-1)}{2}, \sin\dfrac{\pi(i-1)}{2}) & (i=1,....4) \\ \sqrt{2}c(\cos\dfrac{\pi(2i-9)}{4}, \sin\dfrac{\pi(2i-9)}{4}) & (i=5,....8) \end{cases} \quad (2)$$

where c is the lattice speed given by the ratio of the lattice spacing Δx to the time step Δt. It is also related to the sound speed by $c_s = c/\sqrt{3}$.

The LBM algorithm is an iterative process. The evolution of the probability distribution function $f_i(\vec{x}, t)$ at each time step can be obtained by solving the discrete form of the Boltzmann equation:

$$f_i(\vec{x} + \vec{e}_i t, t + \Delta t) - f_i(\vec{x}, t) = \Omega_i(f) \quad (3)$$

where $\Omega_i(f)$ is a collision operator which controls fluid particle collisions at each node. One of the simplest and widely used linearized collision operators was proposed by Bhatnagar *et al.* [34]. It is called BGK, or single-relaxation-time model , and assumes that the density distribution function tends towards an equilibrium function with a single relaxation time τ:

$$\Omega_i^{BGK} = -\frac{1}{\tau}(f_i(\vec{x}, t) - f_i^{eq}(\vec{x}, t)) \quad (4)$$

where f^{eq} is the equilibrium distribution function that reads:

$$f_i^{eq}(\vec{x}, t) = w_i \rho_f (1 + \frac{3}{c^2}\vec{e}_i \cdot \vec{u} + \frac{9}{2c^4}(\vec{e}_i \cdot \vec{u})^2 - \frac{3}{2c^2}\vec{u} \cdot \vec{u}). \quad (5)$$

The weighting factors w_i depend on the discretization scheme. For the present D2Q9 model, $w_0 = \frac{4}{9}$, $w_{1,2,3,4} = \frac{1}{9}$, and $w_{5,6,7,8} =$

$\frac{1}{36}$. The relaxation time τ is a dimensionless parameter and relates to the kinematic viscosity of the fluid ν, the lattice speed c, and the spatial resolution Δx, such as:

$$\tau = \frac{3\nu}{c\Delta x} + \frac{1}{2}. \tag{6}$$

The macroscopic variables of the flow, namely the density and velocity, can be recovered from the distribution function as:

$$\rho_f = \sum_{i=0}^{8} f_i \tag{7}$$

$$\vec{u} = \frac{1}{\rho_f} \sum_{i=0}^{8} f_i \vec{e_i} \tag{8}$$

while the fluid pressure is directly determined by the state equation $P = c_s^2 \rho_f$ in the low Mach number limit, *i.e.* when $M_a = \frac{V_{max}}{c} \leq 0.1$ with V_{max} being the maximum velocity of the fluid flow .

Since the BGK model deals with a unique relaxation time τ, all hydrodynamic variables evolve at the same rate which can be problematic for numerical stability when τ approaches 0.5. Fortunately, there exist alternative collision models, such as two-relaxation-time (TRT) and multiple-relaxation-time (MRT), that can overcome this shortcoming by introducing additional relaxation times. For the simulations presented here, we have chosen the TRT approach where the density distribution functions is separated into symmetric and antisymmetric parts as follows:

$$f_i^+ = \frac{f_i + f_{-i}}{2}, \qquad f_i^- = \frac{f_i - f_{-i}}{2} \tag{9}$$

$$f_i^{eq+} = \frac{f_i^{eq} + f_{-i}^{eq}}{2}, \qquad f_i^{eq-} = \frac{f_i^{eq} - f_{-i}^{eq}}{2} \tag{10}$$

where $-i$ stands for the notation for the vector $\vec{e}_{-i}$ that points to the opposite direction of $\vec{e}_i$ ($\vec{e}_{-i} = -\vec{e}_i$). Each part of the density distribution function then relaxes independently to an equilibrium state and the collision operator in TRT model, can be then computed as:

$$\Omega_i^{TRT} = \frac{1}{\tau^+}(f_i^+ - f_i^{eq+}) - \frac{1}{\tau^-}(f_i^- - f_i^{eq-}) \tag{11}$$

where τ^+ and τ^- are the symmetric and antisymmetric relaxation time, respectively. τ^+ is related to the kinematic viscosity of the fluid via $\nu = \frac{1}{3}(\tau^+ - \frac{1}{2})\Delta x c$, while τ^- is an arbitrary constant that depends on the so-called magic parameter [35]: $\wedge = \left(\tau^+ - \frac{1}{2}\right)\left(\tau^- - \frac{1}{2}\right)$. The latter appears to rule the stability properties of the TRT framework [35] for an optimal value of $\wedge = \frac{1}{4}$. Note that the TRT model simply reduces to the usual BGK scheme when $\tau^+ = \tau^- = \tau$.

3.2. Solid phase modeling: Discrete Element Method (DEM)

The DEM, initially proposed by Cundall and Strack in 1979 [37], has since become an numerical solution for the modelling of particulate systems as rocks or soils.The method relies on a microscopic description of the interactions and motions of an assembly of solid particles whose trajectories are governed by Newton's equations:

$$m_i \frac{\mathrm{d}\vec{u}_i}{\mathrm{d}t} = \vec{F}_i^c + \vec{F}_i^h + m_i \vec{g} \quad (\text{with} \quad \frac{\mathrm{d}\vec{x}_i}{\mathrm{d}t} = \vec{u}_i) \tag{12}$$

$$J \frac{\mathrm{d}\vec{\omega}}{\mathrm{d}t} = \vec{T}_i^c + \vec{T}_i^h \tag{13}$$

where m_i, $\vec{x}_i$ and $\vec{u}_i$ are the particle mass, position and velocity, respectively. $\vec{F}_i^h$ is the hydrodynamic force acting on the particle i (see 3.3 below), $\vec{F}_i^c$ is the resultant contact force from other particles and $\vec{g}$ represents the acceleration due to body forces as gravity. $\vec{T}_i^c$ and $\vec{T}_i^h$ respectively denote the total torque resulting from the inter-particle contact forces and the fluid torque, while J is the momentum of inertia and ω is the angular velocity. The particle position and velocity are solved using a time integration scheme with Verlet algorithm.

Each particle contact force $\vec{F}_i^c$ can be decomposed into a normal component $\vec{F}_{ij}^n$ and a tangential component $\vec{F}_{ij}^t$. The normal component is calculated by a linear viscoelastic Kelvin-Voigt model:

$$F_{ij}^n = -k_n \delta_{ij}^n - \gamma_n v_{ij}^n \tag{14}$$

where k_n is the normal spring stiffness at contact and γ_n is the normal coefficient of viscous dissipation. δ_{ij}^n stands for the overlap accounting for the interpenetration of the two perfectly rigid particles i and j, and v_{ij}^n is the relative velocity in the normal direction. As regards the tangential component of the contact force, it is computed using a viscous-regularized Coulomb model:

$$F_{ij}^t = -\min(k_t \delta_{ij}^t, \mu F_{ij}^n) sgn(\delta_{ij}^t) \tag{15}$$

k_t being the coefficient of regularization and μ the friction coefficient, while δ_{ij}^t denotes the tangential displacement at contact.

The time step given in Eqs.(12) and (13) should be appropriately selected in order to ensure a stable numerical simulation and integrate correctly Newton's equations of motion. Generally, DEM time-step Δt_{DEM} remains sufficiently below a critical value Δt_{cr} which represents the oscillation duration of the spring-mass system that models the particle-particle contacts. Δt_{cr} is thus related to the smallest particle mass m_{min} and the stiffness k_n through:

$$\Delta t_{cr} = 2\pi \sqrt{m_{min}/k_n}. \tag{16}$$

The DEM time step is then chosen as $\Delta t_{DEM} = \lambda \Delta t_{tr}$ with a time-step factor λ selected here around 0.1. Eventually, the normal coefficient of viscous dissipation γ_n can be derived from the coefficient restitution e_n and reads:

$$\gamma_n = \frac{-2 \ln e_n \sqrt{m k_n}}{\sqrt{\pi^2 + \ln^2 e_n}}. \tag{17}$$

3.3. Fluid-solid interactions: coupled LBM-DEM modeling

Coupling LBM and DEM requires a careful account of fluid-solid moving boundaries. To this end, we followed the interpolated bounce-back boundary condition originally proposed by Bouzidi *et al.* [38]. The hydrodynamic force and torque exerted by the flow on a solid particle can be obtained by the following momentum exchange calculation:

$$\vec{F}^h = \sum_{x_f} \sum_i [f_i(\vec{x_f}, t) + f_{-i}(\vec{x_f}, t + \Delta t)]\vec{e}_i. \quad (18)$$

$$\vec{T}^h = \sum_{x_f} \sum_i (\vec{x_w} - \vec{x_c}) \times [f_i(\vec{x_f}, t) + f_{-i}(\vec{x_f}, t + \Delta t)]\vec{e}_i \quad (19)$$

A last consideration concerns the particularity of a 2D granular porous medium which is in fact occluded when the particles are in contact: there is no flow path through the medium and the permeability is virtually zero. To resolve this issue, each solid particle is assumed to have a reduced radius r_h (called hydraulic radius) in the LBM calculation while keeping its real radius r in the DEM calculation. Here, we chose a reasonable ratio of $r_h/r = 0.8$ as suggested by Cui *et al.* [39].

Finally, as each method has its own time-step, it is essential to synchronize them correctly to avoid numerical stability problems. The DEM time-step being usually smaller than the LBM one, several steps of DEM calculation are performed during a unique LBM loop. However, the number of DEM sub-loops must remain low enough otherwise the fixed hydrodynamic quantities given by the preceding LBM calculation may gradually become out of step with the real situation of the system. For all the simulations presented here, this number of DEM sub-loops is set at 2, as a suitable compromise.

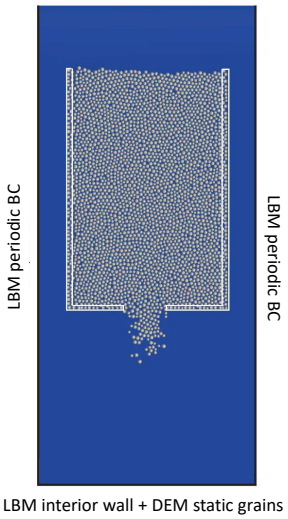

Figure 1: DEM and LBM boundary conditions for the submerged hopper simulations. The particles contained in the white rectangles are assigned to be fixed.

4. Submerged granular flow rates

4.1. Numerical configuration

Numerical simulations of submerged silos were carried out by means of the 2D numerical modeling described above, coupling Lattice Boltzmann Method (LBM) and Discrete Element Method (DEM). More precisely, we have developped in previous works an in-house code, including a parallelized version, that has been validated through the study of different hydromechanical configurations involving soil erosion [32, 12, 25, 42, 43].

For the present study, our numerical model consists in a granular sample composed of 3000 spherical particles fully immersed in a larger fluid domain, as sketched in Figure 1. We simulate two separate samples of particles of mean diameter d=1 mm and d=2 mm. To avoid creating an ordered spheres packing (granular crystallisation), we introduce a slight polydispersity through an uniform particle size distribution characterized by a ratio of 1.5 between the maximum and the minimum particle size. The liquid viscosity varies from 5 to 500 times the one of water. It is worth noting that we actually have to impose a viscosity high enough to limit the fluid velocity magnitude and consequently remains in the low Mach number and almost incompressible limit, as required by the LBM approach. An orifice centered at the bottom of the granular assembly allows the particles to exit out of the silo. For the following parametric study, the orifice diameter D varies from 10 to 30 times the mean diameter d of the grains. At both the lateral and bottom walls (except at the oulet), we fix the corresponding border particles and simultaneously implement in the LBM part of the code, a zero fluid velocity condition. Note that the DEM static condition also concerns the two particles whose centers are located at the edges of the orifice, *i.e.* at the actual distance of $D/2$ from both sides of the middle. Consequently, we point out here that the effective size of the aperture will be assumed to be equal to $(D - d)$ in the following. Regarding the immersion fluid domain, a periodic boundary condition is imposed at the left and right sides while the bottom condition is the same as for the silo's walls. Note that the latter immersion configuration induces a recirculation of the fluid on both sides of the lateral walls of the silo, as will be discussed just after. All simulation parameters are presented in Table 1.

Table 1: DEM-LBM simulation parameters and dimensionless numbers.

	value	unit
Solid phase		
Friction coefficient, μ	0.3	
Rolling coefficient, μ_r	0.3	
Grain density, ρ_s	2.5×10^3	kg/m^3
Grain diameter, d	1.2, 2	mm
Normal stiffness, k_n	1×10^5	N/m
Tangential stiffness, k_t	0.5×10^5	N/m
Rolling stiffness, k_r	$0.1k_n$	N/m
Coefficient of restitution, e_n	0.5	
Fluid phase		
Fluid density, ρ_f	10^3	kg/m^3
Fluid viscosity, ν	$(5 - 500) \times 10^{-6}$	m^2/s
Dimensionless numbers		
Reynolds number, Re	$0.005 - 83$	
Archimedes number, Ar	$0.1 - 4708$	

4.2. Phenomenology

First, we wondered to what extend the fluid recirculation ruled by the hydraulic condition of the present numerical setup influences the granular discharge. To this end, we have tested different configurations: the dry case, by performing a simple DEM simulation, and four submerged cases in which the recirculating flow of the fluid at the both sides of the hopper is limited by interposing a wall of variable opening in the gap between the side walls and the borders of the fluid domain. Figure 2 shows typical behaviors during the submerged discharge for the different opening conditions, namely: a completely impermeable wall, a central one-slot wall with a void fraction φ_w=0.2, a two-slots wall with φ_w=0.4, and a free recirculation condition. When plotting the number of grains escaping from the orifice as a function of time and comparing submerged to dry cases, we first observe a clear decrease of the slope when adding an interstitial fluid. A further decrease in the flow rate is found if the fluid is progressively prevented from recirculating. The mean flow rate Q_{mean}, determined as presented thereafter in 4.3, is thus reduced by almost a factor 6 in the presence of the closed wall. Note that this particular case could actually lead to a complete blockage of the hopper after a much longer simulation duration. Indeed, previous numerical works on similar submerged hoppers have evidenced a regime where a cavity can be stably formed [12, 25], presumably reminiscent to the so-called ticking hourglass [40, 41, 23]. The case with no wall is selected for the rest of the present study (Fig. 1), but this preliminary analysis nonetheless highlights the strong sensitivity to hydraulic boundary conditions, especially regarding fluid recirculation.

In this paper, we are particularly interested in the effect of viscous liquids on the discharge of grains of mean diameter d. As mentioned above, our simulations are restricted to a low Mach number regime by implemented an interstitial fluid that is at least 5 times more viscous than water. Consequently, we focus on the laminar regime at low Reynolds numbers where the latter is defined by $Re = \frac{V_t d}{\nu}$, with V_t the terminal velocity of a single particle of diameter d in the fluid under consideration, at rest. Notice that this velocity needs to be calculated for each parameters set as presented more in detail in the Appendix. Indeed, to our knowledge, there is no equivalent to Stokes law to determine V_t in 2D and, furthermore, the highest Reynolds numbers of the studied range are substantially above the purely viscous regime. To rationalize the fluid-grains coupling, we also propose to consider the Archimedes number which is the ratio of gravitational forces to viscous forces, defined as $Ar = \frac{(\rho_s - \rho_f) g d^3}{\rho_f \nu^2}$. Note that Ar only depends on grain and fluid properties and can interestingly be obtained prior to any simulation result, contrarily to Re that requires V_t to be set. According to the simulation parameters displayed in Table 1, we performed a comprehensive study accross ranges of Ar and Re from 0.025 to 1.708 and 0.005 to 83, respectively.

Figure 3 presents typical simulations of the submerged granular discharge process for different fluid viscosities. The four snapshots have been acquired at different times of the discharge chosen in such a way that the mass lost is similar in all cases. We can observe that one of the main influences of the interstitial fluid is to lower the grains flow rate: the more viscous the fluid, the slower the discharge. The time needed to reach a same loss of grains consistently decreases when the viscosity increases: immersed in a fluid that is 100 times much viscous, the grains flow rate is reduced about a factor 5. In the last section, we will notably present how solid and fluid velocities are closely correlated. More qualitatively, we can observe that the outgoing grains aggregate into a single cluster for the smallest Reynolds number case while more dispersed sedimentating flows are observed for larger Re.

As introduced in Sec. 1, our micro-mechanical approach based on DEM-LBM coupling provides insight into the internal granular structure. Similarly to previous dry silo simulations only based on DEM method [18], the present simulations display the global pattern of stress transmission. When adding a fluid, the contact forces still give rise to unstable arches which alternatively form and vanish during the discharge process. Figure 4 presents the internal grain stress field by calculating the total stress tensor for each grain, as the contribution of both the stress exerted by the neighboring particles in contact and the hydraulic stress of the surrounding fluid. One finding is that the arching structure does not seem to depend substantially on the fluid viscosity. Whereas lubrification in the case of colliding particles is known to play a crucial role [49], there is here no significant impact on the shear contact forces between particles, probably because the present submerged hopper preserves a dense packing during the whole discharge process.

4.3. Discharge flow rate determination

Figure 5 shows the instantaneous solid flow rate Q, obtained by numerical time differentiation of the eroded grains number Nb (see a typical evolution of Nb in Fig. 2) during the whole process. Contrarily to the dry case where a plateau is almost reached till the beginning of the discharge [48], there is here an

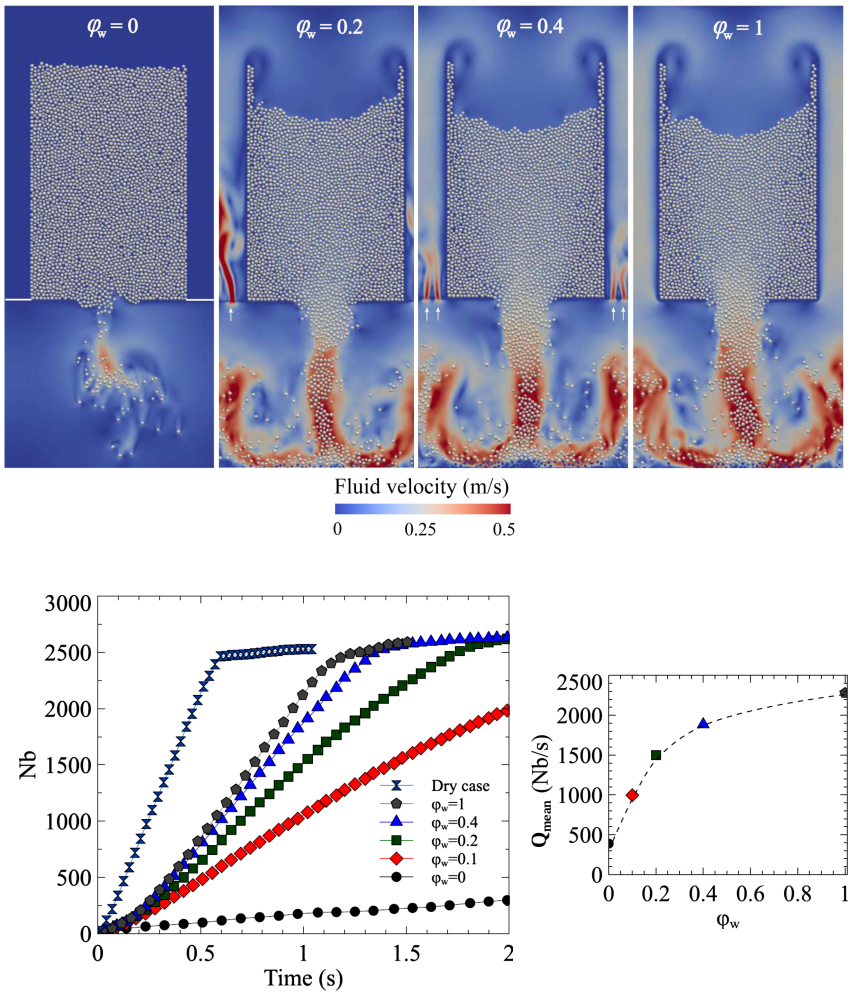

Figure 2: (Top) Submerged hopper simulations for particles diameter of d = 1.2 mm, orifice size of D/d=20 and fluid viscosity of $\nu = 10^{-5}$ m^2/s, according to different hydraulic conditions imposed by varying void fractions φ_w (from left to right): impermeable wall, a wall including one slot, a wall including 2 slots, and no-wall. (Bottom left) Number of grains flowing through the orifice as a function of time. (Bottom right) Mean flow rate as a function of φ_w. The dotted line is only a guide for the eyes.

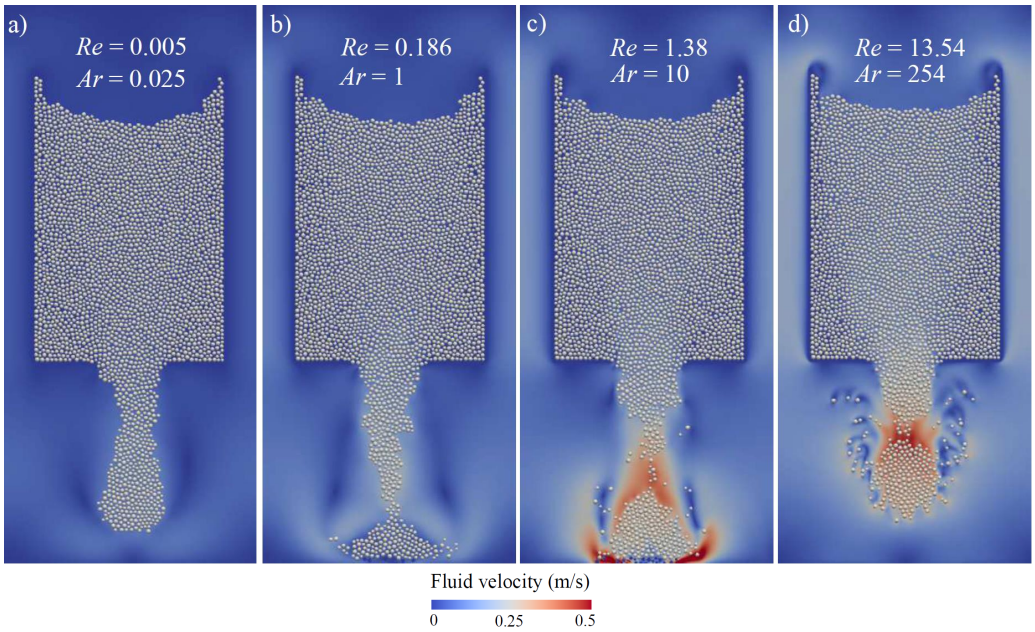

Figure 3: Snapshots of submerged hopper simulations for particles diameter of d = 1.2 mm, orifice size of D/d=20 and different fluid viscosities: a) $\nu = 10^{-3}$ m^2/s at t= 1.79 s, b) $\nu = 1.6 \times 10^{-4}$ m^2/s at t=0.69 s, c) $\nu = 5 \times 10^{-5}$ m^2/s at t=0.51 s, d) $\nu = 10^{-5}$ m^2/s at t=0.35 s. The color scale indicates the fluid velocity.

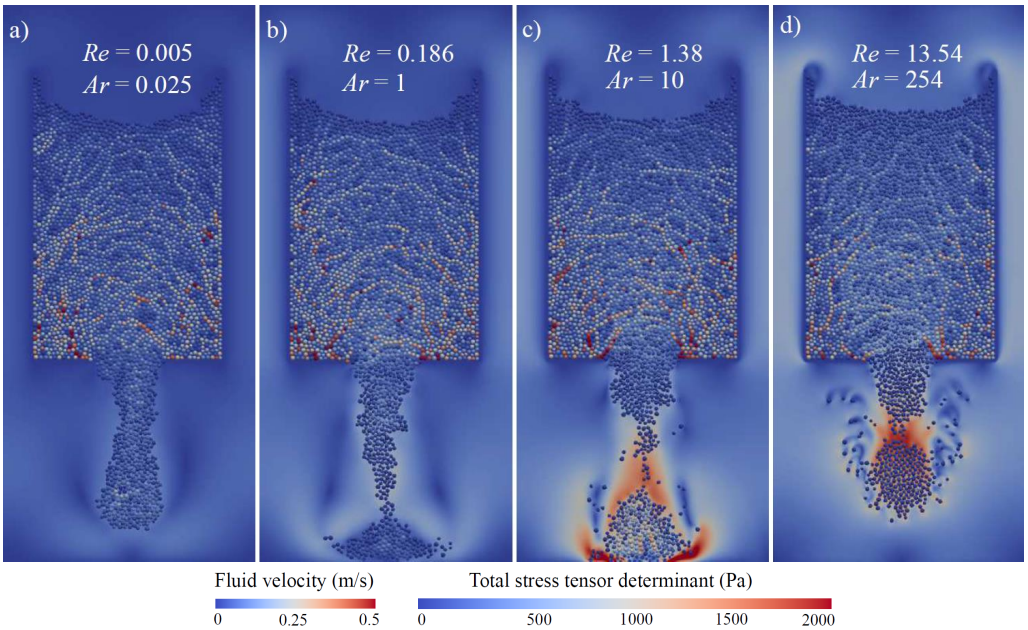

Figure 4: Snapshots of the same simulations than in Fig. 3 by displaying the total stress tensor determinant.

initial and rather long acceleration phase which makes it harder to quantify Q. Qualitatively, this discharge flow curve can be separated into three domains: a first increase, a plateau-like behavior, and a decrease corresponding to the final emptying of the silo. To perform a systematic post-processing, the maximal flow rate Q_{max} is first detected and next used to determine the times t_1 and t_2 when $Q = 0.5Q_{max}$. The mean flow rate Q_{mean} is finally evaluated by averaging in the range $t_1 < t < t_2$ (see Fig. 5a). From the time evolution of Q for different Ar plotted in Fig. 5b, we observe a simple proportional relation between Q_{mean} and Q_{max} giving confidence to our approach (see inset in Fig. 5b).

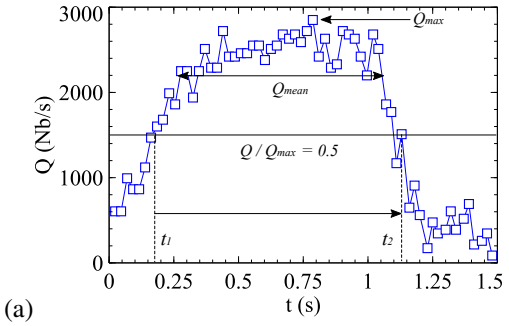

Figure 5: Typical evolution of the instantaneous solid flow rate for $d = 1.2$ mm and D/d=20. (a) Mean and maximum flow rate determination for $\nu = 5 \times 10^{-5}$ m^2/s. (b) Q *versus* time for various fluid viscosities. Inset: Q_{max} *versus* Q_{mean}. The dashed line stands for $y = 1.2x$

Even more interestingly we found that this time evolution of Q is almost self-similar since all the curves approximately collapse when ploting $\frac{Q}{Q_{mean}}$ as a function of $\frac{t}{t_2}$, as shown in Figure 6. Consistently with the self-similarity, t_1 and t_2 are indeed found to be roughly proportional to each other, namely $t_2 \approx 5t_1$, and both are approximately inversely proportional to Q_{mean} as is expected from mass conservation (see inset in Fig. 6 for t_2). Note that the present temporal collapse includes however a slight discrepancy between the cases with particle diameters d=1.2 mm and d=2 mm. In addition, it is observed that the curve starts to slightly depart from the collapse for the smallest Ar values.

4.4. Beverloo law revisited

For dry non-cohesive grains, the solid discharge flow rate from an outlet of size D in the bottom of a hopper is accurately

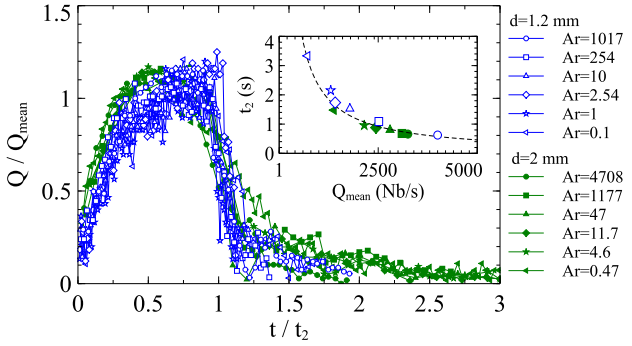

Figure 6: Normalized flow rate Q/Q_{mean} as a function of t/t_2 for the whole set of simulations. Inset: t_2 as a function of Q_{mean}. The dashed line is a guide for the eyes.

described by the empirical Beverloo law given in Eq. (1). Wilson *et al.* [24] experimentally studied the transient arching in play in a submerged context. Unlike the dry case, the characteristic grain exit velocity is found to be set by the terminal falling velocity V_t (instead of the grain free-fall velocity), giving the following revisited law for the mass flow rate:

$$\dot{M}^{3D} = C\rho_s V_t (D - kd)^2 \tag{20}$$

For the present DEM-LBM modelling of a 2D submerged hopper, we can logically propose to transpose Eq. (20) from 3D to 2D, such as:

$$\dot{M}^{2D} = C\rho_s V_t (D - kd) \tag{21}$$

Then, considering that $\dot{M}^{2D} = Q(\rho_s \pi d^2/4)$, the discharge flow rate Q (in Nb/s) can be written as:

$$Q = C\frac{4}{\pi d} V_t (D/d - k) \tag{22}$$

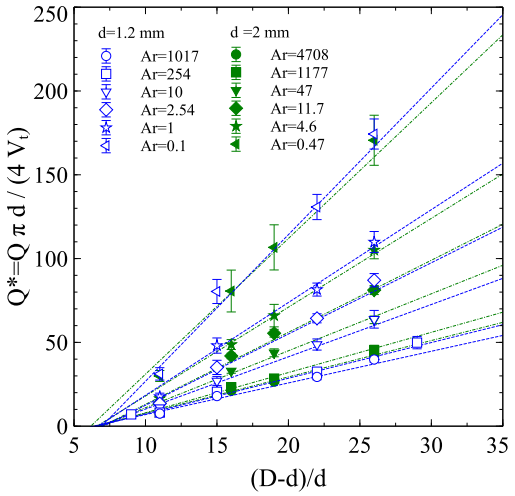

Figure 7: Dimensionless $Q^* = Q\pi d/4V_t$ as a function of the dimensionless effective aperture $(D-d)/d$, for the whole set of simulations. The lines indicate linear fits.

In Figure 7, for all our simulations, we plot the solid flow rate normalized by $\frac{4V_t}{\pi d}$, $Q^* = Q\pi d/4V_t$ as a function of the

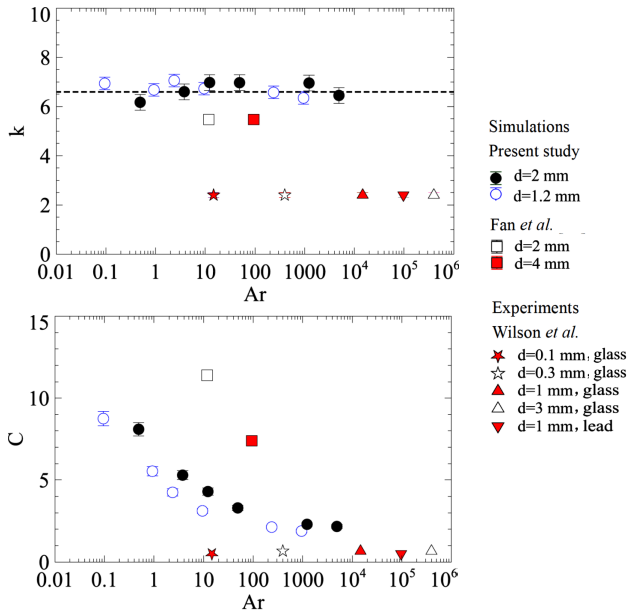

Figure 8: Parameters k and C of the 2D Beverloo law as a function of the Archimede numbers Ar, for the present simulations, a previous numerical study by Fan *et al.* [25], and experiments by Wilson *et al.* [24].

effective aperture size which is not D, but $(D-d)$ (see the detailed numerical configuration description in 4.1), divided by the particle diameter d. As expected, we observe linear correlations when fixing both the fluid viscosity and the grain size or, equivalently, for a given Ar value. According to Eq. (22), we can obtain the parameters k and C of the revisited Berverloo law by linear regression. Figure 8 displays the latters as a function of the Archimedes number Ar. On the one hand, we find that the coefficient k is almost constant over the whole range of Ar with an average value equal to k=7.0 ± 0.2. This value is well higher than 1.5 as usually found for the dry spherical grains, confirming that the addition of an interstitial fluid decreases significantly the apparent orifice size. By comparison, the experiments by Wilson *et al.* performed on lead and glass spherical beads of various sizes [24], gave a Beverloo cut-off k around 2.4. This discrepancy could be attributed to the restricted 2D dimension of our simulations. Then, if confronting the present results with our previous 2D submerged hopper simulations for which the numerical configuration (hydraulic condition, granular sample dimension) differs susbstantially [25], we consistently got a closer value of k around 5.5. On the other hand, Fig. 8 presents a coefficient C that decreases approximately from 10 to 2.5 with Ar over five decades. In [24], the different measurements lead to C values under 1. Once again, the 2D-3D intrinsic differences could be responsible for these discrepancies. In [25], the simulations gave values of C that are systematically higher, certainly due here again to the distinct hydrodynamic conditions, but with a similar decrease as Ar increases.

Within this first approach to the problem, we have restricted our analysis to a Beverloo-like frame, by predicting the solid flow rates in the submerged case for a large range of Archimedes numbers which is of practical interest. However, this approach remains empirical and based on the concept of transient arching which has recently been strongly questioned, notably by more local measurements of particle flowsat the outlet [20, 45, 46]. In the next section, we propose to focus on the submerged discharge at the grains' scale.

5. Fluid-grains coupling

5.1. Grains velocity profiles

Thanks to the Discrete Element Method (DEM) used to simulate the solid phase, the outgoing grains velocity profiles can be calculated at the outlet orifice for different dimensionless apertures D/d, ranging from 10 to 30, and for different fluid viscosities ν, ranging from 10^{-5} to 10^{-4} m^2/s. Practically, we focus on the discharge process around its maximum flow rate Q_{max} by only considering the times when $Q \geq 0.9Q_{max}$. During this period, we first acquired the velocity of each particle which passes through the aperture, *i.e.* whose center is vertically located at the orifice level and horizontally located inbetween $D/2$ from both sides of the central axis. We then proceeded to a local space averaging in order to get a regularly spaced x-axis for the velocity profiles. Some illustrative curves are shown in Fig. 9a. The maximum of the velocity, denoted by V_c, reached at the center of the orifice, increases with D/d at constant viscosity but get lower when viscosity is higher. Compared to the terminal velocity V_t (calculated by direct simulations as presented in the appendix), V_c is found to be systematically higher, from about 1.2 to 4.4 times for the cases presented in Fig. 9b. The ratio V_c/V_t increases with D/d and decreases with ν. A specific analysis on the correlation between these two characteristic grains velocities is proposed in the next subsection.

Irrespective of D/d and ν, the profiles all have a similar parabolic shape. In Figure 10, these profiles can be directly compared plotting $V^* = V/V_c$ as a function of $x^* = 2x/(D-d)$. Let's indeed remind that the actual outlet size is $(D-d)$ instead of D, because the two particles at the edges of the orifice are fixed (see more details in 4.1). This normalization clearly induces a gathering into a single curve. Exactly as for the 2D-dry case that was experimentally and numerically studied in [20, 44, 46], we observe a collapse consistent with a parabolic profile $V^* = \sqrt{1-x^{*2}}$. This self-similarity of the profiles suggests that the picture proposed for the dry hopper discharge is still relevant in the present submerged situation. Admittedly, we can assume the existence of a dynamic arch supported on both edges of the outlet orifice, and consider that the grains fall from this domed roof. To explore this physical interpretation further, we acquired different velocity profiles adimensionalized by the terminal velocity V_t, at earlier times of the discharge process (see Figure 11). Each velocity profile results from the average over the duration indicated in the corresponding temporal evolution (see inset in Fig. 11). Interestingly, as the flow increases until it reaches its maximum rate, the profile evolves from a plug to the parabolic shape presented above, by displaying a velocity at the center that goes from a value very close to the

terminal velocity V_t, to a value 3 times higher (previously defined as V_c). This typical plug-like behavior at the beginning of the discharge is perfectly in line with the picture of a unique grain sedimenting in a fluid at rest, characterized by V_t which is independent of the free-fall height. Then, as the entrainment of the surrounding fluid grows in importance, the grains velocity varies along the aperture such as reaching the parabolic self-similar profile described in Fig. 10.

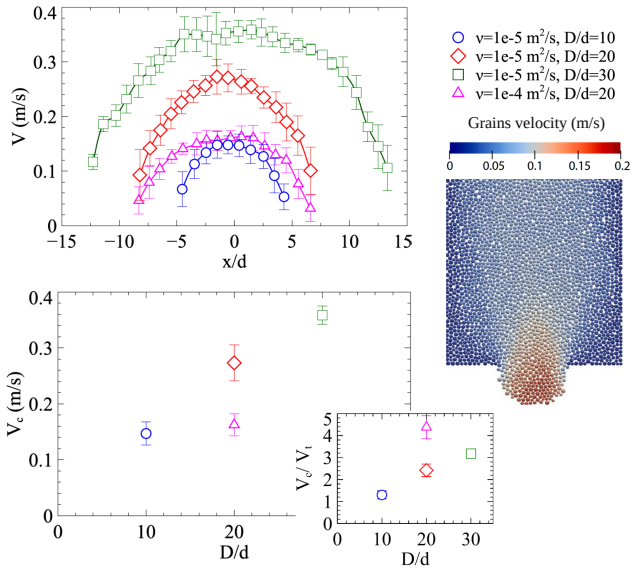

Figure 9: (Top) Typical velocity profiles for d=1.2 mm, various fluid viscosities and orifice sizes. For clarity, the standard deviation is included only for a single data set. (Bottom) The velocity at the center of the orifice V_c as a function of D/d. Inset: Normalized velocity V_c/V_t *versus* D/d. (Right) DEM visualization for the grains velocity.

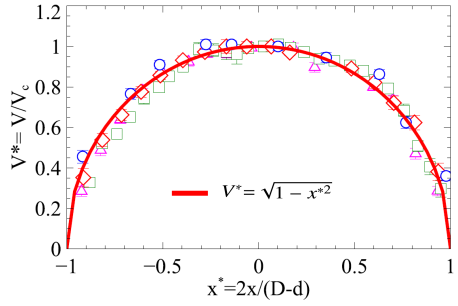

Figure 10: Normalized velocity profiles $V^*(x^*)$ of the same simulations than in Fig. 9 and the scaling function (see text for details).

5.2. *Fluid entrainment*

The main interest of the present work, among the numerous hopper-related studies, is to consider the effect of a viscous interstitial fluid on the grains discharge. From a micromechanical point of view, adding a complex particle-fluid interaction modifies the grains contact conditions and raises new questions regarding the underlying mechanism. Immersion typically makes

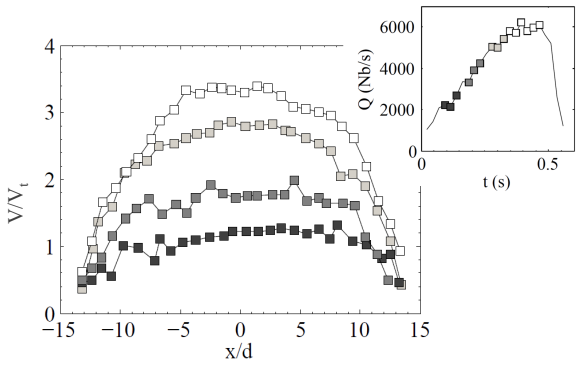

Figure 11: Normalized velocity profiles V/V_t for d=1.2 mm, $\nu = 5 \times 10^{-5}$ m^2/s and D/d=30, at different times of the discharge process. Inset: Temporal evolution of the corresponding flow rate Q (same symbols and colors than in the main graph).

the system overdamped and leads to a substantial dissipation of the grains kinetic energy by the fluid [28]. Consequently, at the macro-scale, we have indeed observed a significant slowdown of the solid flow rate as the fluid viscosity increases (see Sec. 2, Fig. 3). In this last part, we focus on a more local scale, by investigating the fluid entrainment to be related to the two characteristic grain velocities defined above, namely the maximum velocity reached at the center of the exit orifice V_c and the terminal velocity V_t.

In Figure 12, we thus plotted the outlet Reynolds number $Re_c = \dfrac{V_c d}{\nu}$ as a function of the corresponding Archimedes number. Despite some scattering, all the points gather into a single trend. By comparison with the semi-empirical law predicted for Re defined from the terminal velocity V_t (see Eq. (A.4) in Appendix), we observe a systematic upward shift, but an overall agreement. This strong correlation between V_c and V_t (or equivalently Re_c and Re) suggests that the underlying mechanism of submerged hoppers is physically-based on the free-fall of a single particle under the action of both buoyancy and drag forces. We also ascertain that the measurements coming from a recent experimental work of Koivisto & Durian [26] on underwater silos of beads are correctly placed among our numerical data.

Let's now adapt the theory to the situation where the fluid is no more at rest but has its own velocity V_f due to the entrainment effect of the downward moving particles. Assuming that V_f, at the exit, is simply proportional to the grain velocity V, i.e. $V_f = \alpha V$, the analytical development proposed in the Appendix remains almost the same except that the relative velocity is now $V_r = V - V_f = (1-\alpha)V$. So that the new terminal velocity, which is *a priori* equal to V_c, is directly given by: $(1-\alpha)V_c = V_t$, where V_t is still the expression given in the Appendix for the terminal velocity when the surrounding fluid is at rest. From this realtion, we can calculate the fluid entrainment coefficient: $\alpha = 1 - V_t/V_c$ whose values are easily deduced from the whole set of simulations. As can be seen on Figure 13a, the data are somehow scattered when plotted as a

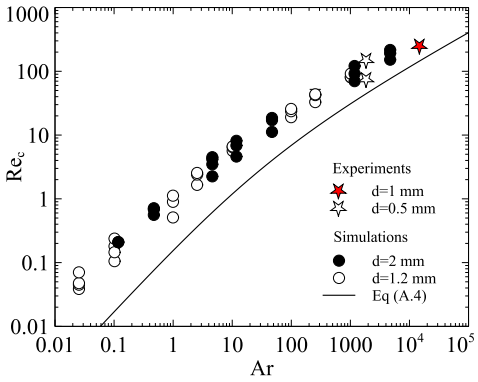

Figure 12: Reynolds numbers Re_c defined with the maximum velocity V_c, as a function of Archimedes numbers Ar for the whole set of simulations data, and experiments from [26]. The solid line stands for the semi-empirical law for Re defined with V_t, predicted by the 2D free-fall theory (see Appendix).

function of the dimensionless outlet size D/d, whereas we observe a rather satisfactory collapse into a decreasing function over about five decades when plotting α *versus* the Archimedes number Ar, as presented in Fig. 13b. In addition, the experimental data reported in [26] for underwater hopper discharges of spherical particles are in a good agreement with our numerical results, giving consistency to the scaling. We can finally notice that α tends to 1 when $Ar \ll 1$. This asymptotic limit is consistent with the fact that a very viscous liquid becomes almost impossible to shear leading to a collective downward fall of both solid and liquid phases. As a short-term perspective, we plan to acquire straigthforwardly the fluid velocity V_f, in order to directly evaluate the fluid entrainment coefficient $\alpha = V_f/V$. But giving the granular dense packing, the acquisition of interstitial fluid LBM-data would certainly required significant efforts in terms of post-processing.

6. Conclusion

This work was based on a numerical approach coupling the discrete element method and the lattice Boltzmann method to model the discharge from 2D-hoppers of grains totally immersed in a viscous liquid. First, we observed that the main influence of the fluid viscosity, in a broad range going from 5 to 500 times the one of water, was to slowdown the solid flow rate. It was notably highlighted a high sensitivity to the hydraulic boundary conditions, which control the fluid recirculation from outside to inside of the hopper. Contrarily to dry case where the steady regime of discharge is quickly reached, the submerged case exhibits a solid flow rate that increases very gradually to a plateau, followed by a decreasing phase during the final emptying of the silo. This specific time evolution was interestingly found to be approximately self-similar. Considering the mean discharge flow rate, we demonstrated through an exhaustive parametric study that the revisited Beverloo law for the submerged condition proposed by Wilson *et al.* [24] is indeed applicable. However, the corresponding cut-off parameter k and flowability coefficient C are found substantially higher than in the dry case and also in the experimental sub-

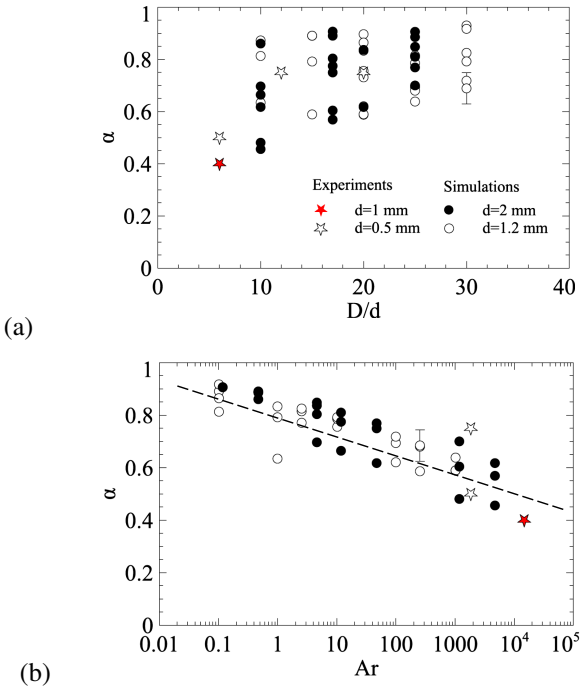

Figure 13: Fluid entrainment coefficient $\alpha = 1 - V_t/V_c$ as a function of D/d for the whole set of simulations. (b) Same data plotted *versus* Ar. The experimental data are obtained from [26]. The dashed line in (b) is only a guide for the eyes.

merged condition. We presume that this is due to both the limitation of the 2D modelling and the impact of the interstitial liquid. Regarding the latter which is quantified by the Archimedes number Ar, we observed that the parameter k is almost constant when Ar varies over 5 decades, while the coefficient C decreases with Ar.

Focusing next on the role of fluid-grains interactions, we have demonstrated the presence of a self-similar velocity profile for the exiting grains at the orifice, exactly as for the dry case. At the first moments of the discharge, the grains exhibit a plug-like profile with a maximum velocity almost equal to the terminal velocity V_t. Then, the shape of the profiles are becoming progressively parabolic, with an outlet velocity V_c reached at the center of the orifice that is systematically greater than V_t. We believe this comes from the fact that, when falling downwards, the grains entrain the surrounding fluid in their movement in a more or less pronouced extent. A final analysis proposed to estimate this fluid entrainment by using the parameter $\alpha = 1 - V_t/V_c$. We thus demonstrated that α decreases from 1 in the very low Ar regime (i.e. for the viscous limit where the grain and the fluid velocities are the same) to about 0.5 for Ar values corresponding to water environment, in consistency with recent experiments [26].

In future work, the present numerical results require being confirmed by experiments in a broad enough range of Archimedes numbers, necessitating significant variation in grains (diameter, density) and fluid (viscosity) properties. Although the global mechanism that drives the submerged hopper has been discussed here, a number of questions regarding

this phenomenon are still open, in particular in the unsteady regime, where the local poro-mechanical coupling of such dilatating dense granular flows appears as a rich and complex issue.

Appendix: 2D-analysis for the terminal velocity

Theoretically, the steady regime of a single particle free-falling in a surrounding fluid is reached when the particle buoyancy is balanced by the fluid drag. The corresponding relation in 2D is:

$$(\rho_g - \rho_f) g \frac{\pi d^2}{4} = \frac{1}{2} \rho_f d C_d V_t^2 \tag{A.1}$$

where V_t is the terminal velocity of the particle and C_d is the drag coefficient which varies according to the hydrodynamic conditions. Then, by introducing both the Reynolds number $Re = \dfrac{V_t d}{\nu}$ and the Archimedes number $Ar = \dfrac{(\rho_s - \rho_f) g d^3}{\rho_f \nu^2}$, the drag coefficient C_d simply reads:

$$C_d = \frac{\pi}{2} Ar / Re^2 \tag{A.2}$$

Using our 2D DEM-LBM code, we directly simulate a unique particle falling under gravity in a fluid, for the same conditions than the ones covered in the present parametric study of submerged hoppers (see all parameters in Table 1). Figure A.1 displays the drag coefficient C_d, deduced from the terminal velocity V_t, as a function of Re. By adjusting these data to a trend line, we propose the following empirical law with good accuracy:

$$C_d(Re) = \left[\left(\frac{4}{5} \right)^{\frac{3}{5}} + \left(\frac{9}{Re} \right)^{\frac{3}{5}} \right]^{\frac{5}{3}} \tag{A.3}$$

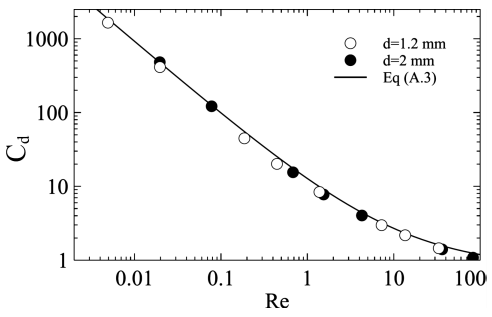

Figure A.1: Drag coefficient C_d obtained from direct simulations of a single particle falling in a viscous fluid as a function of $Re = \dfrac{V_t d}{\nu}$. The line stands for the empirical law in Eq. (A.3).

By combining Eq. (A.2) and Eq. (A.3), it comes a second-order equation for $X = Re^{\frac{3}{5}}$:

$$X^2 + X \left(\frac{45}{4} \right)^{\frac{3}{5}} - \left(\frac{5\pi}{8} Ar \right)^{\frac{3}{5}} = 0.$$

We thus get a semi-empirical expression for the Reynolds number as a function of the Archimedes number, such as:

$$Re = \left[\sqrt{\left(\frac{5\pi}{8} Ar \right)^{\frac{3}{5}} + \frac{1}{4} \left(\frac{45}{4} \right)^{\frac{6}{5}}} - \frac{1}{2} \left(\frac{45}{4} \right)^{\frac{3}{5}} \right]^{\frac{5}{3}} \tag{A.4}$$

Or, alternatively:

$$Re = \frac{45}{4} \left(\frac{1}{2} \right)^{\frac{5}{3}} \left[\sqrt{1 + \left(\frac{Ar}{Ar_c} \right)^{\frac{3}{5}}} - 1 \right]^{\frac{5}{3}} \tag{A.5}$$

with the introduction of the critical Archimedes number $Ar_c = \frac{1.6}{\pi} \left(\frac{45}{4} \right)^2 \left(\frac{1}{4} \right)^{\frac{5}{3}} \simeq 6.4$. Note the two limit behaviors:

- when $Ar \ll Ar_c$, $Re = \frac{\pi}{18} Ar \simeq 0.17 Ar$
- when $Ar \gg Ar_c$, $Re = \sqrt{\frac{5\pi}{8} Ar} \simeq 1.40 \sqrt{Ar}$

[1] W.A. Beverloo, H.A. Leniger, J. Van de Velde, The flow of granular solids through orifices, Chem. Eng. Sci. 15 (1961) 260269. https://doi.org/10.1016/0009-2509(59)80042-7.

[2] J.A.H. De Jong, Q.E.J.J.M Hoelen (1975). Cocurrent gas and particle flow during pneumatic discharge from a bunker through an orifice. Powder Technology, 12(3), 201-208.

[3] R.M. Nedderman, U. Tzn, S.B. Savage, G.T. Houlsby, The flow of granular materials-I. Discharge rates from hoppers, Chem. Eng. Sci. 37 (1982) 15971609. https://doi.org/10.1016/0009-2509(82)80029-8.

[4] R. Brown, Minimum energy theorem for flow of dry granules through apertures. Nature 191, 458461 (1961). https://doi.org/10.1038/191458a0

[5] R.M. Nedderman, C. Laohakul, The thickness of the shear zone of flowing granular materials, Powder Technol. 25 (1980) 91100. https://doi.org/10.1016/0032-5910(80)87014-8.

[6] A.A. Mills, S. Day, S. Parkes, Mechanics of the sandglass, Eur. J. Phys. 17 (1996) 97109. https://doi.org/10.1088/0143-0807/17/3/001.

[7] G.F Sowers, Building on sinkholes: design and construction of foundations in karst terrain. American Society of Civil Engineers. 1996.

[8] T. Waltham, Sinkhole hazard case histories in karst terrains. Quarterly Journal of Engineering Geology and Hydrogeology, 41, 291-300 (2008) http://dx.doi.org/10.1144/1470-9236/07-211

[9] G. Noury, J. Perrin, L.H. Luu, P. Philippe, S. Gourdier. Role of floods on sinkholes occurence in covered karst terrains: case study of Orléans area (France) during the 2016 meteorological event and perspectives for other karst environments. In 15th Multidisciplinary Conference on Sinkholes and the Engineering and Environmental Impacts of Karst (2018).

[10] D. Ford, P. Williams, Introduction to Karst, in: Karst Hydrogeol. Geomorphol., John Wiley & Sons, Ltd, 2007: pp. 18. https://doi.org/https://doi.org/10.1002/9781118684986.ch1.

[11] B. Beck, Soil Piping and Sinkhole Failures, in: W.B. White, D.C. Culver (Eds.), Encycl. Caves, Second Edition, Academic Press, Amsterdam, 2012: pp. 718723. https://doi.org/https://doi.org/10.1016/B978-0-12-383832-2.00106-7.

[12] L.H. Luu, G. Noury, Z. Benseghier, P. Philippe, Hydro-mechanical modeling of sinkhole occurrence processes in covered karst terrains during a flood, Eng. Geol. 260 (2019) 105249. https://doi.org/https://doi.org/10.1016/j.enggeo.2019.105249.

[13] K. Wieghardt, Experiments in granular flow, Annu. Rev. Fluid Mech. 7 (1975) 89114. https://doi.org/10.1146/annurev.fl.07.010175.000513.

[14] C.S. Campbell, Granular material flows - An overview, Powder Technol. 162 (2006) 208229. https://doi.org/10.1016/j.powtec.2005.12.008.

[15] J. Tang, R.P. Behringer, Orientation, flow, and clogging in a two-dimensional hopper: Ellipses vs. disks, Europhys. Lett. 114 (2016) 34002. https://doi.org/10.1209/0295-5075/114/34002.

[16] H. An, X. Wang, X. Fang, Z. Liu, C. Liang, Wall normal stress characteristics in an experimental coal silo, Powder Technol. 377 (2021) 657665. https://doi.org/https://doi.org/10.1016/j.powtec.2020.09.016.

[17] P.A. Langston, U. Tuzun, D.M. Heyes, Discrete element simulation of internal stress and flow fields in funnel flow hoppers, Powder Technol. 85 (1995) 153169. https://doi.org/https://doi.org/10.1016/0032-5910(95)03009-X.

[18] S. Masson, J. Martinez, Effect of particle mechanical properties on silo flow and stresses from distinct element simulations, Powder Technol. 109 (2000) 164178. https://doi.org/10.1016/S0032-5910(99)00234-X.

[19] W.R. Ketterhagen, J.S. Curtis, C.R. Wassgren,& B.C. Hancock (2009). Predicting the flow mode from hoppers using the discrete element method. Powder technology, 195(1), 1-10.

[20] A. Janda, I. Zuriguel, D. Maza, Flow rate of particles through apertures obtained from self-similar density and velocity profiles, Phys. Rev. Lett. 108 (2012) 15.

[21] S. Guo, T. Yu, Y. Zhang (2017). Water-submerged granular flow through a long efflux tube. Granul. Matter. 9(3), 18.

[22] Y. Zhou, P.Y. Lagrée, S. Popinet, P. Ruyer, P. Aussillous (2019). Gas-assisted discharge flow of granular media from silos. Physical Review Fluids, 4(12), 124305.

[23] B. K. Muite, M.L. Hunt, G.G. Joseph (2004). The effects of a counter-current interstitial flow on a discharging hourglass. Physics of Fluids, 16(9), 3415-3425.

[24] T.J. Wilson, C.R. Pfeifer, N. Meysingier, D.J. Durian, Granular discharge rate for submerged hoppers, Pap. Phys. 6 (2014).

[25] J. Fan, L.H. Luu, G. Noury, P. Philippe, DEM-LBM numerical modeling of submerged cohesive granular discharges, Granul. Matter. 22 (2020) 115. https://doi.org/10.1007/s10035-020-01035-9.

[26] J. Koivisto, D.J. Durian, The sands of time run faster near the end, Nat. Commun. 8 (2017) 16. https://doi.org/10.1038/ncomms15551.

[27] J. Koivisto, M. Korhonen, M. Alava, C.P. Ortiz, D.J. Durian, A. Puisto, Friction controls even submerged granular flows, Soft Matter. 13 (2017) 76577664. https://doi.org/10.1039/c7sm00806f.

[28] J. Koivisto, D.J. Durian, Effect of interstitial fluid on the fraction of flow microstates that precede clogging in granular hoppers, Phys. Rev. E. 95 (2017) 32904. https://doi.org/10.1103/PhysRevE.95.032904.

[29] L. Rondon, O. Pouliquen, P. Aussillous, Granular collapse in a fluid: Role of the initial volume fraction, Phys. Fluids. 23 (2011) 73301. https://doi.org/10.1063/1.3594200.

[30] K. Kumar, J.-Y. Delenne, K. Soga, Mechanics of granular column collapse in fluid at varying slope angles, J. Hydrodyn. Ser. B. 29 (2017) 529541. https://doi.org/https://doi.org/10.1016/S1001-6058(16)60766-7.

[31] F. Lominé, L. Scholtès, L. Sibille, P. Poullain, Modeling of fluid-solid interaction in granular media with coupled lattice Boltzmann/discrete element methods: application to piping erosion, Int. J. Numer. Anal. Methods Geomech. 37 (2013) 577596. https://doi.org/10.1002/nag.

[32] J. Ngoma, P. Philippe, S. Bonelli, F. Radjai, J.Y. Delenne, Two-dimensional numerical simulation of chimney fluidization in a granular medium using a combination of discrete element and lattice Boltzmann methods, Phys. Rev. E. 97 (2018) 124. https://doi.org/10.1103/PhysRevE.97.052902.

[33] Y.H. Qian, D. D'Humières, P. Lallemand, Lattice BGK models for Navier-Stokes equation, Europhys. Lett. 17 (1992) 479484.

[34] P.L. Bhatnagar, E.P. Gross, M. Krook, A model for collision processes in gases. I. Small amplitude processes in charged and neutral one-component systems, Phys. Rev. 94 (1954) 511525.

[35] I. Ginzburg, D. d'Humières, A. Kuzmin, Optimal stability of advection-diffusion lattice boltzmann models with two relaxation times for positive/negative equilibrium, J. Stat. Phys. 139 (2010) 10901143. https://doi.org/10.1007/s10955-010-9969-9.

[36] Q. Zou, X. He, On pressure and velocity boundary conditions for the lattice Boltzmann BGK model, Phys. Fluids. 9 (1997) 1591. https://doi.org/10.1063/1.869307.

[37] P.A. Cundall, A discrete numerical model for granular assemblies, Geomechanics. 29 (1979) 4765.

[38] M. Bouzidi, M. Firdaouss, P. Lallemand, Momentum transfer of a Boltzmann-lattice fluid with boundaries, Phys. Fluids. 13 (2001) 34523459. https://doi.org/10.1063/1.1399290.

[39] X. Cui, J. Li, A.H.C. Chan, D.N. Chapman, A parametric study on the leakage-soil interaction due to a leaking pipe using the coupled DEM-LBM technique, AIP Conf. Proc. 1542 (2013) 10351038. https://doi.org/10.1063/1.4812111.

[40] T. Le Pennec, K.J. Maloy, A. Hansen, M. Ammi, D. Bideau & X.L. Wu(1996). Ticking hour glasses: experimental analysis of intermittent flow. Physical Review E, 53(3), 2257.

[41] C.T. Veje, P. Dimon (2001). The dynamics of granular flow in an hourglass. Granular matter, 3(3), 151-164.

[42] Z. Benseghier, P. Cuéllar, L.H. Luu, J.Y. Delenne, S. Bonelli, P. Philippe, Relevance of free jet model for soil erosion by impinging jets. J. Hydraul. Eng. 146(1), 04019047 (2020)

[43] Z. Benseghier, P. Cuéllar, L.H. Luu, S. Bonelli, P. Philippe, A parallel GPU-based computational framework for the micromechanical analysis of geotechnical and erosion problems, Comput. Geotech. 120 (2020) 103404. https://doi.org/10.1016/j.compgeo.2019.103404.

[44] A. Bhateja, Velocity scaling in the region of orifice influence in silo draining under gravity, Phys. Rev. E. 102 (2020) 42904. https://doi.org/10.1103/PhysRevE.102.042904.

[45] M.A. Madrid, J.R. Darias, L.A. Pugnaloni (2018). Forced flow of granular media: Breakdown of the Beverloo scaling. EPL (Europhysics Letters), 123(1), 14004.

[46] F. Alonso-Marroquin, P. Mora (2021). Beverloo law for hopper flow derived from self-similar profiles. Granular Matter, 23(1), 1-8.

[47] A.M. Cervantes-Alvarez, S. Hidalgo-Caballero, F. Pacheco-Vázquez (2018). The simultaneous discharge of liquid and grains from a silo. Physics of Fluids, 30(4), 043302.

[48] A. Anand, J.S. Curtis, C.R. Wassgren, B.C. Hancock, W.R. Ketterhagen (2009). Predicting discharge dynamics of wet cohesive particles from a rectangular hopper using the discrete element method (DEM), Chem. Eng. Sci. 64 52685275. https://doi.org/10.1016/j.ces.2009.09.001.

[49] J.A. Simeonov, J. Calantoni (2012). Modeling mechanical contact and lubrication in direct numerical simulations of colliding particles. International Journal of Multiphase Flow, 46, 38-53.